Volume 34 | Number 10 | October 2019 | Pages 1945–2150

JAAS

Journal of Analytical Atomic Spectrometry

rsc.li/jaas

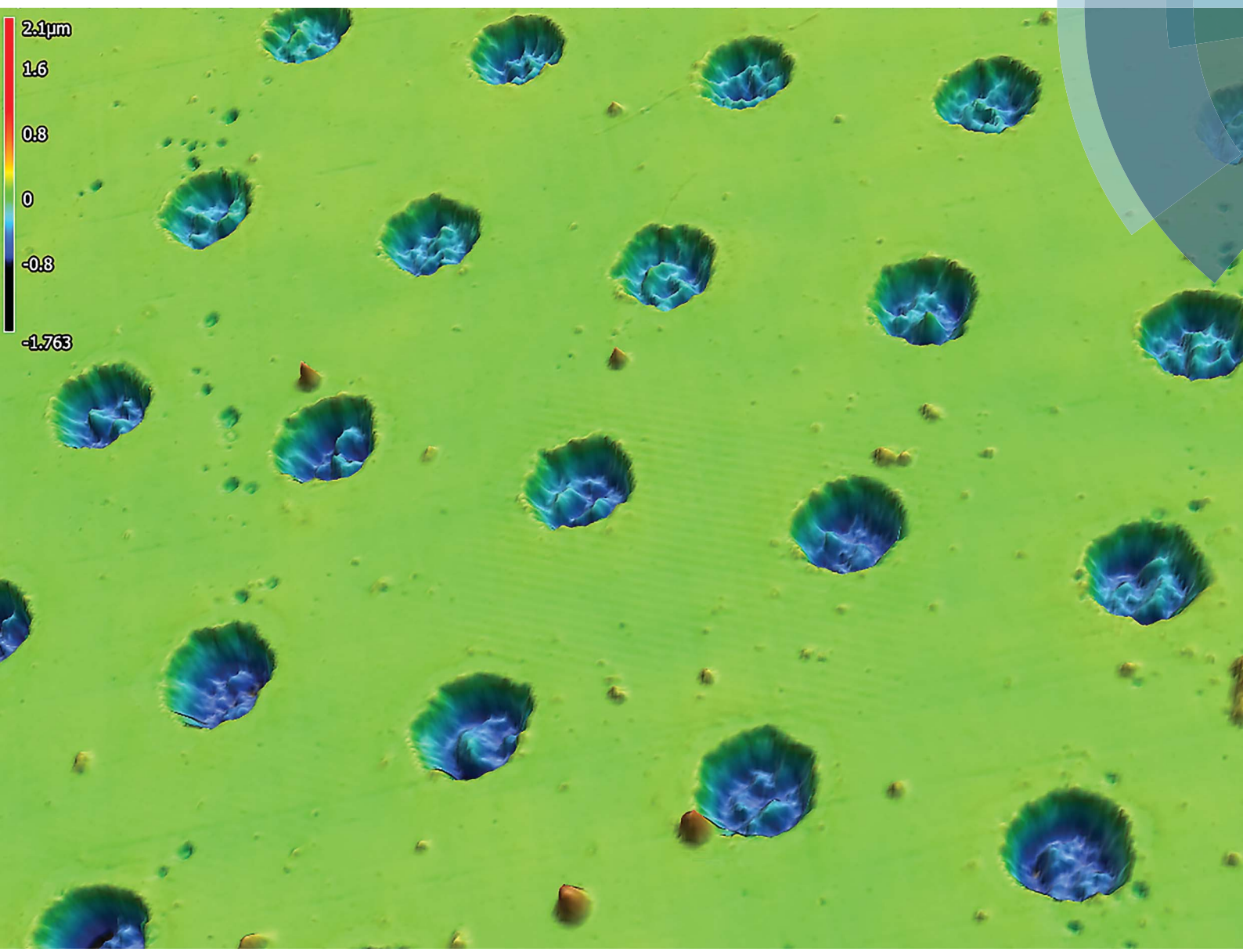

ISSN 0267-9477

ROYAL SOCIETY OF CHEMISTRY | Celebrating IYPT 2019

PAPER

M. Krachler *et al.*

Single shot laser ablation MC-ICP-MS for depth profile analysis of U isotopes in UO_2 single crystals

JAAS

PAPER

View Article Online
View Journal | View Issue

Cite this: J. Anal. At. Spectrom., 2019, 34, 1965

Single shot laser ablation MC-ICP-MS for depth profile analysis of U isotopes in UO_2 single crystals

M. Krachler, *[a] A. Bulgheroni,[a] A. I. Martinez Ferri,[a] Y. Ma,†[b] A. Miard[b] and Ph. Garcia[b]

An analytical procedure for determining the $n(^{235}U)/n(^{238}U)$ amount ratio in consecutive layers of UO_2 single crystals was developed and validated. A 25 μm circular shaped laser beam with a fluence of only 0.24 J cm^{-2} was employed for depth profiling ^{235}U and ^{238}U in UO_2 single crystals with U isotopes being detected *via* MC-ICP-MS. The time-resolved ^{235}U and ^{238}U MC-ICP-MS signals obtained from individual laser shots were processed automatically using software specifically developed for this purpose. Downhole fractionation of the $n(^{235}U)/n(^{238}U)$ amount ratio was excluded by shooting 80 laser pulses on a reference UO_2 single crystal of known composition, revealing no measurable change in its U isotopic ratio during depth profiling. A linear relationship between the number of laser shots and the average depth of the laser ablation craters was established using confocal laser scanning profilometry. The ns-laser ablation system produced conical craters whose diameters were shown to increase with the number of laser pulses. The shape and roughness of the craters were studied as a function of both the number of pulses and focusing conditions. Using a dual beam focused ion beam (FIB), high resolution scanning electron microscopy (SEM) micrographs revealed the formation of rectangular "tiles" on the reference UO_2 single crystal after as little as five laser shots. The ordered, rectangular structure disappeared progressively with increasing number of laser pulses, while simultaneously a sub-micrometric porosity developed. The depth profiling capabilities of the laser ablation system were applied to two UO_2 single crystals produced under different experimental conditions involving solid state isotopic mixing of ^{235}U and ^{238}U in order to characterise U self-diffusion in UO_{2+x}. Both UO_2 single crystals featured a $n(^{235}U)/n(^{238}U)$ ratio gradient, containing enriched U at the surface and depleted U in the bulk.

Received 19th June 2019
Accepted 16th July 2019

DOI: 10.1039/c9ja00212j

rsc.li/jaas

Introduction

The study of uranium dioxide (UO_2) single crystals is often a necessary starting point for determining nuclear oxide fuel bulk properties, as they constitute a yardstick against which actual nuclear fuels, used on an industrial scale, may be assessed.[1] Because single crystal samples are deemed homogeneous and to have a well-defined crystal structure on a macroscopic scale, they enable materials scientists to study underlying physical mechanisms. This allows them in certain cases to apply their findings to more complex structures such as polycrystalline sintered UO_2 pellets prior to, during or following in-reactor irradiation.[1]

It is essential to study uranium self-diffusion as it is thought to control many key engineering properties such as creep, sintering, and fission product behaviour that are all very important to several stages of the nuclear fuel cycle. Further a systematic study of this property provides an insight into the characteristics of uranium point defects which is difficult to do any other way as these defects are present in the material only in very small quantities.[1]

Nowadays, the accurate and precise determination of the elemental and/or isotopic composition of advanced crystalline materials is of utmost importance to guarantee their properties and to identify potential contaminants.[2–12] Classical analytical approaches employing dissolution of a fragment of such materials followed by subsequent chemical analysis are not effective because their features are captured either in thin (nm to μm thick) layers or within local hot spots. Therefore, solid sampling techniques such as Electro-Thermal Vaporisation (ETV) or Laser Ablation (LA) are employed frequently for this purpose.[7] LA-based techniques additionally offer easy access to spatially resolved information on the elemental/isotopic composition of the investigated material.

While the use of other surface analytical techniques such as secondary ion mass spectrometry (SIMS), glow discharge-mass spectrometry (GD-MS), X-ray photoelectron spectroscopy (XPS) or transmission electron microscopy (TEM) may also be

[a]European Commission – Joint Research Centre Karlsruhe, P.O. Box 2340, D-76125 Karlsruhe, Germany. E-mail: michael.krachler@ec.europa.eu

[b]CEA, DEN, DEC, Centre de Cadarache, 13108 Saint-Paul-lez-Durance, France

† Current address: Sino-French Institute of Nuclear Engineering and Technology, Sun Yat-Sen University, Zhuhai 519082, P. R. China.

advantageous within this context, LA combined with ICP-MS has found widespread use during the last decade.[7] The benefits of LA-ICP-MS include easy manipulation of samples under atmospheric pressure as well as providing both high spatial resolution and high sensitivity because specimens are analysed directly.[7] The lateral resolution of a few μm enables identifying potential inhomogeneity within a sample, with extended line scan analysis providing results reflecting bulk analysis.[11,12] In addition, depth profiling capabilities of LA provide sub-μm depth resolution.[4,6–8]

Despite all of its advantages, LA-ICP-MS suffers from some important limitations such as non-uniform ablation processes and matrix-dependent melting events.[6,8] These drawbacks are known to be less prominent for fs-LA units compared to their ns-counterparts.[3] Employing laser beam homogenisers, thereby converting the Gaussian beam profiles into flat-top beam profiles, further improvements of the analytical performance have been achieved.[8,13]

Depth profiling may suffer from so-called downhole fractionation (DHF), mainly caused by differences in the volatility and chemical properties of the measured elements.[14,15] For a given number of laser pulses, this phenomenon occurs earlier in small-diameter laser spots (greater depth/width ratio) compared to large-diameter spots.

Even though the use of a two-volume LA cell largely accelerates washout of the generated particle plume,[4,6,14] the lowest repetition rate of the LA system and/or the minimum selectable acquisition time of the ICP-MS instrument might hinder the independent acquisition of analytical signals generated by subsequent laser pulses. If these technical restrictions are overlooked, mixing of neighbouring material layers may occur thereby deteriorating the depth resolution. To circumvent this issue, measurement protocols recording single shot events have been applied successfully.[16]

Combining a ns-LA unit and MC-ICP-MS, this study aims to develop an analytical procedure for depth profiling UO_2 single crystals with respect to their $n(^{235}U)/n(^{238}U)$ ratio. The complementary use of confocal laser scanning profilometry and high resolution scanning electron microscopy (SEM) micrographs, obtained by using a dual beam focused ion beam (FIB), contributed largely to the understanding of the laser/material interaction.

Experimental

Instrumentation

Laser ablation MC-ICP-MS. A ns-laser ablation (LA) system from ESI Lasers (Bozeman, MT, U.S.A.), operated at a wavelength of 213 nm, was employed for the removal of small amounts of material from the investigated solid samples. For improved analytical performance a two-volume laser ablation cell (TV2 cell) and He as a carrier gas were used. Further experimental details were reported earlier.[10–12]

The Faraday detectors of a double-focusing multi-collector inductively coupled plasma mass spectrometer (MC-ICP-MS, Nu Plasma™, NU Instruments, Wrexham, Wales, U.K.) measured the abundance of ^{235}U and ^{238}U in the ablated particle cloud. Before switching to LA, the MC-ICP-MS was tuned for sensitivity and stability of U signals in solution mode employing an aqueous 30 ng L^{-1} U calibration solution having natural U isotopic composition. The key parameters of the entire LA-MC-ICP-MS set-up are summarised in Table 1. Additional information can be found elsewhere.[10–12] A minimum of five sets of LA-MC-ICP-MS experiments were conducted for each parameter reported in this study. The signal intensities of ^{235}U and ^{238}U were recorded with the time-resolved-analysis option of MC-ICP-MS software.

TIMS. After acid dissolution of a small fraction of the investigated reference UO_2 single crystal, isotope dilution-mass spectrometry using TIMS was employed to determine the abundance of ^{235}U and ^{238}U following accredited analytical procedures.

Confocal laser scanning profilometer. Surface characterisation of the investigated samples was performed using a 16-bit 3D laser scanning confocal microscope (Keyence VK-X250/X260) with a 408 nm (violet) laser wavelength. A confocal laser beam was rastered over the field of view and the reflected light, filtered by a pin-hole, was collected on a 16-bit photomultiplier. For each image pixel, the focal distance (vertical *z*-axis) was determined. The reflected laser light was collected and recorded on a photomultiplier; the *z*-position corresponding to the maximum of this distribution was assigned to the pixel as its average height.

Employing the highest magnification objective (150×), a field of view of 95 μm × 70 μm was acquired within a few seconds with a theoretical *z*-resolution of 0.5 nm, a repeatability of 7 nm and a lateral resolution of 120 nm. Several slightly overlapping images were stitched together to obtain a larger field of view.

Surface roughness. The high resolution height measurement of the confocal laser scanning profilometer was utilised to determine the surface roughness of both the pristine sample surface and the bottom of the ablation crater. While there are several definitions of surface roughness, the surface arithmetical mean height (Sa) was selected to characterise the above-mentioned surfaces in this study.

Table 1 Selected operating conditions of the LA-MC-ICP-MS setup for depth-resolved U isotopic measurements using individual laser shots

LA parameters	
Wavelength	213 nm
Fluence	0.24 J cm^{-2}
Spot diameter, circular	25 μm
Ablation frequency	1 Hz, single shots
Carrier gas	He, 170 mL min^{-1}
Acquisition parameters	
Isotopes measured	^{235}U and ^{238}U; both on Faraday detectors
Background	60 s
Integration time	200 ms per data point
Time between laser shots	10 s
Number of replicates	5

Average step depth. In order to measure the depth of each laser crater and to calculate the ablation rate, the average step depth of each crater was established after having corrected the sample surface for tilting and spherical deformation. In this context, the term step refers to the fact that the average heights of two surfaces are compared to each other, with one of the two being the reference level. The average step depth approach provided a more robust indicator than the much simpler line profile due to the increased roughness and the inhomogeneity of the crater bottom.

Dual beam focused ion beam (FIB) microscope. A ThermoFisher Scientific Versa 3D dual beam FIB was used for both microscopic imaging and slice-and-view analysis. It featured a 30 kV FEG electron gun for high resolution scanning electron imaging and a 30 kV Ga liquid metal ion source for milling (*i.e.* sputtering) and fine-polishing of the investigated UO_2 single crystals. The electron and the ion columns were mounted at 38° degrees allowing for simultaneous recording of electron and ion generated images. Such tilted images were useful in revealing surface deformation.

The advantage of having the ion gun is evident when the sample underneath the crater position has to be studied; in fact, a trench can be milled inside the crater to reveal a cross-sectional view of the sample just below the ablated level. Ion currents as high as 3 nA were used for coarse trench milling, while distinctly lower currents (down to 30 pA) were applied for fine-polishing of the cross-section.

Investigated uranium samples

Reference UO_2 single crystal. A single crystal of UO_2, hereafter named SC1, was selected as a "reference material" for this study because of numerous advantages compared to its corresponding poly-crystalline equivalent. In fact, the extremely reduced porosity of a single crystal as well as the absence of both different crystallographic orientations and a grain size distribution simplify the understanding of the laser/sample interaction.

Macroscopic UO_2 single crystals were retrieved from experimental activities carried out in 1987 at the JRC-Ispra FARO (Furnace And Release Oven) experimental facility in which severe reactor accidents were simulated by out-of-pile experiments.[17] The UO_2 single crystal used in this study was taken from a larger piece with an irregular shape and an original mass of ~25 g from which several 2 mm thick slices were prepared. The ⟨100⟩ crystal direction was established using an X-ray Laue camera. Prior to LA-MC-ICP-MS analysis, the sample surface of the UO_2 single crystal was fine-polished using mono-dispersed diamond suspensions with a decreasing grain diameter down to 1 μm.

UO_2 single crystals with ^{235}U gradients. In order to further test the depth profiling capability of the employed LA system, two additional UO_2 single crystals were prepared with similar ^{235}U enrichment gradients along their thickness (hereafter named SC2 and SC3). In order to produce this isotopic concentration gradient, several drops of a highly ^{235}U enriched aqueous uranyl nitrate solution were deposited on the surface of each of the UO_2 single crystals which were allowed to dry completely. Following a preliminary low temperature heat treatment intended to convert the nitrate to oxide, both samples were heated at 1500 °C for 24 hours at a well-defined oxygen partial pressure (~9×10^{-13} atm for SC2 and ~5×10^{-12} atm for SC3) in order to allow ^{235}U to diffuse into the UO_2 single crystal matrix. A detailed description of the preparation of these samples is out of the scope of this study and is provided elsewhere.[1] While the crystal orientation of both samples was identical, it was not aligned with one of the main crystal directions. Fitting the corresponding Laue images revealed a maximum misalignment of 11° with respect to the ⟨100⟩ direction established for the reference UO_2 single crystal.

LA-MC-ICP-MS measurement protocol

To automate single laser shot analysis and to reduce operator intervention as much as possible,[15] the following measurement protocol was developed and used throughout all time-resolved experiments:

- At the start of each analysis the background signal of both ^{235}U and ^{238}U was recorded for 60 s.
- Prior to each ablation, the laser was allowed to warm up for 8 s, firing at 1 Hz, before the shutter was opened for one second.
- After a single laser shot the shutter was subsequently closed with the laser warming up again for 8 s before releasing the next laser shot. This way, an automated procedure was set-up that produced a single laser shot about every 10 s.
- The generated ^{235}U and ^{238}U ion currents were recorded with the time-resolved software of the MC-ICP-MS.
- The raw data thus obtained were imported into home-made data evaluation software that automatically searched for the generated ^{235}U and ^{238}U signals and further processed the data as described in detail below.

Single shot analysis data evaluation software

The software of the MC-ICP-MS acquired the time-resolved ^{235}U and ^{238}U signals employing an integration time of 200 ms per data point. Because both U isotopes were measured simultaneously, the assignment of a unique timestamp to each measurement point was possible.

Ad-hoc software developed in-house enabled us to analyse the time-resolved MC-ICP-MS signals generated by each individual laser shot. After having subtracted the baseline, calculated as the average of the signals obtained throughout the first 60 s, an automated peak search procedure was performed on the ^{238}U data stream, employing a minimum signal threshold of 200 mV. For each peak, the following information was identified:

- $^{238}U_{max}$: maximum peak height
- t_{max}: timestamp corresponding to $^{238}U_{max}$
- t_-, t_+: timestamps corresponding to the lower and upper limit of the identified peak. For this analysis $\Delta t = t_+ - t_- = 10$ s.

Subsequently, the software calculated the $n(^{235}U)/n(^{238}U)$ amount ratio using the integral R_i, as given in eqn (1).

$$R_i = \frac{\int_{t_-}^{t_+} {}^{235}U(t)dt}{\int_{t_-}^{t_+} {}^{238}U(t)dt} \quad (1)$$

Being a multi-collection system, the timescale was identical for ^{235}U and ^{238}U MC-ICP-MS signals. However, all specific timestamps (t_-, t_+ and t_{max}) were defined considering the ^{238}U signal only. Additionally, a merit index was applied to each laser pulse to identify ^{238}U signals that exceeded the maximum input range (11 V) of the digitizer, or where the ^{235}U signals were too close to the noise level of the Faraday detectors (<5 mV).

The software produces a reduced dataset, containing only the laser pulse index, t_{max} and R_i. Using these data, a depth calibration could be established based upon the pulse index and the laser ablation rate.

Quality control

For the main purpose of this study, no mass bias correction was applied to any of the raw data. However, the certified reference material CRM U-020 (~2 wt% enriched in ^{235}U) was measured repeatedly to obtain an evaluation of potential inaccuracy of the measured U isotope ratio. The experimental $n(^{235}U)/n(^{238}U)$ amount ratio of 0.02069 ± 0.00014 (N = 206) agreed well with the corresponding certified value of 0.02081 ± 0.00020. Similarly, repeated measurements (N = 241) of the $n(^{235}U)/n(^{238}U)$ amount ratio of 0.002228 ± 0.000032 for the reference UO_2 single crystal matched reasonably well with the corresponding amount ratio of 0.0021494 ± 0.0000057 measured *via* isotope dilution mass spectrometry. Consequently, both LA-MC-ICP-MS and isotope dilution mass spectrometry results indicated that the reference UO_2 single crystal contains ~0.22 wt% of ^{235}U.

Results and discussion

Influence of laser ablation parameters on the generated MC-ICP-MS signal

The bulk of the three investigated UO_2 single crystals consisted of depleted (either ~0.2 wt% or ~0.4 wt% ^{235}U) U. The principal goal of this study – to obtain highly resolved depth profiles of the $n(^{235}U)/n(^{238}U)$ amount ratio – created some striking boundary conditions for potential parameters for the LA set-up. First, a MC-ICP-MS maximum signal was required to remain within the linear region of the Faraday detector response signal. To this end, ^{238}U signals were kept below 11 V. Second, low ^{235}U signals had to simultaneously remain detectable using a Faraday detector. This was challenging at times because of the depleted nature of the UO_2 materials. By selecting laser parameters appropriately, the above-mentioned difficulty was well controlled. Enlarging the laser spot size, for example, increased the MC-ICP-MS signals if ^{235}U signals were too low to be measured reliably. Adjusting the MC-ICP-MS signal to 4–8 V for the more abundant U isotope also allowed the reliable measurement of the less abundant U isotope using a Faraday detector. Generating a shorter but higher "intensity pulse" of the MC-ICP-MS by increasing the He gas flow of the LA unit, for instance, was not aimed at because this approach frequently led to high ion currents that exceeded the linear range of the Faraday detector. Only time-resolved ^{235}U signals with a maximum of at least 5 mV were considered in the evaluation of the $n(^{235}U)/n(^{238}U)$ amount ratio for all experiments.

Faraday detectors were selected to measure both ^{235}U and ^{238}U because this type of detector provides much higher precision compared to secondary electron multipliers (SEM). However, Faraday detectors require relatively high signals to overcome their internal electrical noise. Small signals may be preferably measured using an SEM, but its required dead time correction and non-linear behaviour limit the obtainable overall measurement precision. Employing a Faraday detector to measure one U isotope while using a SEM for the other low abundant U isotope suffers from the fact that the relative gain between both detectors varies randomly and therefore limits the achievable measurement precision.

The selected diameter of the laser beam at a given laser fluence determined the intensity of the MC-ICP-MS signal, providing an increasing response with larger spot diameters. The laser fluence, in turn, dictated the UO_2 sputtering rate of the laser beam into the investigated UO_2 materials. The lower the fluence, the less material was removed from the solid samples with a single laser shot. The selected fluence has been considered the most critical parameter for any spatially resolved LA analysis.[3] One of the main challenges in the determination of U isotopic abundance profiles lies in achieving a high spatial resolution. As a result and considering the intensity restrictions mentioned above, a circular laser beam was selected for all experiments with a 25 μm diameter and a laser fluence of ~0.24 J cm^{-2} (0.4% of the nominal maximum laser power). At such low fluences, fluctuations may be expected that are liable to have an essential impact on the laser ablation rate.[8]

Compared to our previous work,[10–12] the carrier gas of the LA unit was changed from Ar to He in this study. The use of He instead of Ar is known to change the aerosol expansion and to improve the transport efficiency.[3] Employing He as the carrier gas, the ICP-MS signal arrived within ~1 s at the detector (as compared to ~15 s with Ar) after the laser shot and returned to the background after about 2 s (~10–15 s with Ar). This fast response and wash-out of the MC-ICP-MS signal was an important feature to avoid mixing of information obtained from subsequent laser shots, *i.e.,* different sample layers. Consequently, the use of He was also conducive to a greater depth resolution.

In the same vein, laser repetition rates had to be sufficiently low to prevent mixing of U signals originating from different laser shots. High laser repetition rates of up to 100 Hz in combination with ultra-fast wash-out LA chambers have been successfully utilised for fast and highly spatially resolved LA-ICP-SFMS analysis for imaging of elemental distributions in single cells and rat retina tissue.[18,19] This experimental approach, however, requires a high ICP-MS acquisition rate. Such fast acquisition rates of 2 ms per isotope were obtained for ICP-sector field MS,[18] however, ICP-time-of-flight MS might be preferable for multiple isotope analysis.[18,20] Even though the TV2 laser ablation cell employed in this study provided a fast

washout, the electronics of the MC-ICP-MS limited the lowest acquisition rate to 200 ms per data point.

As a consequence, even though signals of ^{235}U and ^{238}U were acquired simultaneously in this study, the lowest possible laser repetition rate of 1 Hz was not sufficiently low to completely separate two consecutive U signals when the laser was operated continuously at this low repetition rate. Therefore, a single shot approach was favoured over continuous laser operation. Together with the TV2 laser ablation cell, guaranteeing a fast wash-out of the particle plume from the LA, well separated MC-ICP-MS signals from individual laser shots were obtained. Applying this single laser shot approach, different Faraday detector response times that can potentially lead to bias in the measured U isotope ratio of transient signals during LA, did not need to be considered.[21–23] In other words, integrating the entire signal for both ^{235}U and ^{238}U from the before-shot baseline to the after-shot baseline will not result in a systematic offset of the measured $n(^{235}U)/n(^{238}U)$ amount ratios.[16]

Evaluating downhole fractionation

The measured $n(^{235}U)/n(^{238}U)$ amount ratio associated with a given depth profile can suffer from so-called matrix-dependent downhole fractionation (DHF).[13,14] Generally speaking, for a given ablation time, when using small laser spot sizes, DHF can become an issue even for shallow craters. As the laser spot size increases, DHF will only become an issue at larger crater depths. To guarantee that the data generated throughout this study were not influenced by this phenomenon, 80 laser pulses (fluence 0.24 J cm^{-2}) with a beam diameter of 25 μm were shot on the reference UO_2 single crystal and the $n(^{235}U)/n(^{238}U)$ amount ratio was measured in all 80 sub-samples.

This experiment, repeated on five different laser spots, revealed no measurable fractionation. To this end, the $n(^{235}U)/n(^{238}U)$ amount ratio was plotted *vs.* pulse number for all five measurement series. Each of the plots was fitted with a straight line yielding an average slope of 5×10^{-8} per pulse. In other words, assuming that the linear regression is valid, one would expect a variation of the $n(^{235}U)/n(^{238}U)$ amount ratio of as little as 1‰ only after 20 thousand laser pulses. As only up to 40 laser pulses were required to reach the bulk isotope ratios for actual sample analyses (SC2 and SC3), DHF can be excluded in this study.

Laser ablation rate and crater bottom roughness

To determine crater depths using laser scanning profilometry, groups of five craters were ablated with an increasing number of laser pulses on the reference UO_2 single crystal SC1. This experiment was conducted at three different fluence-per-shot settings, *i.e.,* with 0.24 J cm^{-2}, 0.48 J cm^{-2}, and 1.2 J cm^{-2}, respectively. The average depth (±standard errors) of each group of craters was plotted as a function of the cumulative fluence in Fig. 1A. To arrive at a cumulative fluence of ~20 J cm^{-2}, the corresponding maximum number of laser shots needed varied from 16 for a fluence of 1.2 J cm^{-2} to 80 for a fluence of 0.24 J cm^{-2}.

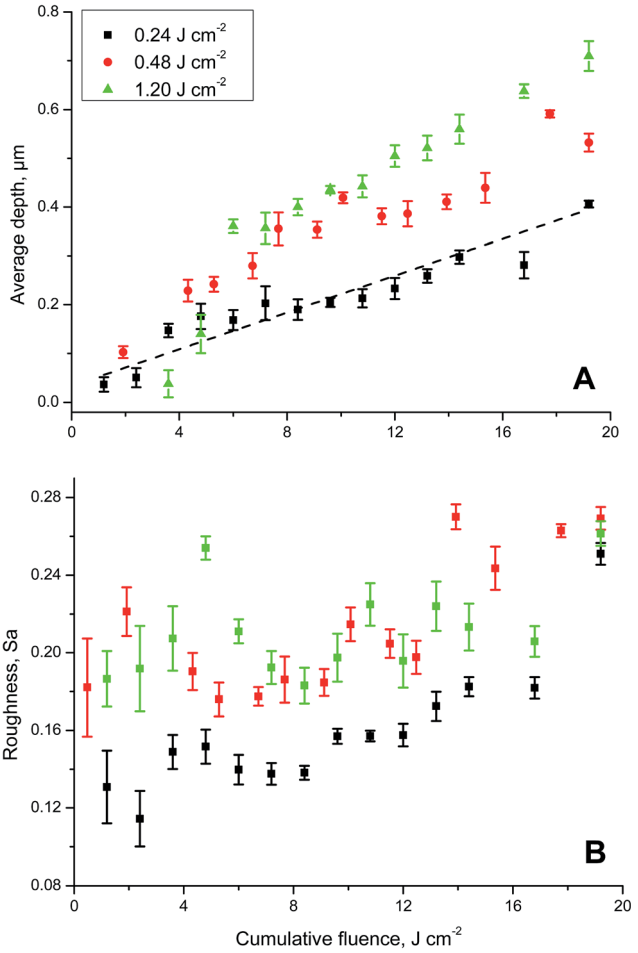

Fig. 1 Impact of the number of laser pulses – represented as cumulative fluence – shot on UO_2 single crystals on the generated ablation craters. (A) Average depth ($n = 5$) of ablation craters of the reference UO_2 single crystal SC1 as a function of cumulative fluence. Experiments were carried out using three different fluence settings, *i.e.,* 0.24 J cm^{-2}, 0.48 J cm^{-2} and 1.20 J cm^{-2}, highlighting the dependency of the laser ablation rate on the energy of the applied laser pulses. (B) Behaviour of surface roughness as a function of the cumulative fluence at various fluence levels.

For all three series of different fluence settings, a linear relationship between the average depth and cumulative fluence was searched for (Fig. 1A). While all data points were considered for fluence settings of 0.24 J cm^{-2} and 0.48 J cm^{-2}, for the highest fluence setting of 1.20 J cm^{-1} linearity did not start before 7 J cm^{-2} (Fig. 1A). The aim of fitting the experimental values was to highlight the potential linear behaviour of depth (Fig. 1A) and surface roughness (Fig. 1B) of the laser ablation craters with increasing fluence. Generally, the slope of the linear regression curves increased with increasing single shot fluence, as summarised in Table 2. This somewhat counterintuitive behaviour can be explained by taking into account the non-linearity of the LA process.[6] Compared to the slope obtained with a fluence of 0.24 J cm^{-2}, this parameter was ~45% greater for experiments carried out with fluence settings of 0.48 J cm^{-2} or 1.20 J cm^{-2} (Table 2).

Table 2 Calculation of laser ablation rates (μm × cm^2 × J^{-2}) at three different fluence settings

Fluence, J cm^{-2}	Min.	Max.	Intercept	Std. error	Slope	Std. error
0.24	0	20	0.0330	0.0146	0.0189	0.0011
0.48	0	20	0.0835	0.0269	0.0277	0.0021
1.20	7	20	0.1645	0.0251	0.0280	0.0023

Increased roughness of the crater bottom is expected as the number of laser pulse increases.[6] However, this parameter remained relatively constant for the reference UO_2 single crystal (Fig. 1B). There appears to be a slight tendency for the surface roughness Sa to increase with cumulative fluence for experiments conducted with a single shot fluence of 0.24 J cm^{-2}. At higher fluences (0.48 J cm^{-2} or 1.2 J cm^{-2}), the surface roughness is somewhat greater, but no clear trend with increasing cumulative fluence is evident (Fig. 1B).

The confocal laser scanning profilometer employed here offers a clear advantage *versus* contact stylus-based systems[6] because no part of the instrument is physically touching and thereby possibly altering the sample surface and thus no artefacts are expected due to the stylus head size. While an Atomic Force Microscope (AFM) will provide superior vertical resolution, the acquisition speed for a large surface is definitively in favour of the laser system employed in this study. Moreover, compared to other optical based techniques (triangulation and white light interferometry), the results of the confocal laser system are not affected by the reflectivity of the sample surface.

Microscopic analysis of the laser interaction with the UO_2 single crystal

Focused ion beam (FIB) investigations help better understand the 3-dimensional microstructure of solid materials.[24] For a deeper insight into the way the laser beam interacts with UO_2 single crystals, several high resolution SEM micrographs of the reference UO_2 single crystal SC1 were acquired along with cross-sectional images taken after FIB milling of lateral trenches (Fig. 2).

After fives laser pulses each with a fluence of 0.24 J cm^{-2}, the sample surface was characterised by the formation of large rectangular "tiles" (Fig. 2). The size of these tiles was larger in the centre of the crater than at its periphery. Some tiles were detached completely from the UO_2 single crystal, while others were bent and about to be released from the sample surface with the next laser pulse. In the vicinity of the ablation craters, several tiles of medium (1 × 1 μm) and large (3 × 3 μm) size were identified, possibly because not all of these tiles were removed efficiently by the helium gas flow passing through the LA chamber. The ordered, rectangular structure progressively disappeared with increasing number of laser pulses as is evident from the micrographs recorded after 40 laser pulses (Fig. 2).

Another noticeable effect of the laser/UO_2 single crystal interaction was the formation of sub-micrometric porosity, present at particularly high concentrations in the periphery of the laser crater. This porosity was unquestionably generated by the laser/sample interaction because it was not visible in the pristine material, neither on the surface nor in the bulk of the reference UO_2 single crystal as revealed by the FIB cross-sections in Fig. 2. A similar behaviour was also observed during SIMS ion sputtering and generally speaking, during corrosion experiments (data not shown), possibly caused by the presence of local defects in the crystal structure.

From cross-sectional images (Fig. 2, right column), it was evident that cavities were formed below the tiles, even below the ones that still appeared to be attached firmly to the substrate. This effect, along with the bending of the large tiles that were about to be removed with the subsequent laser pulse, is the

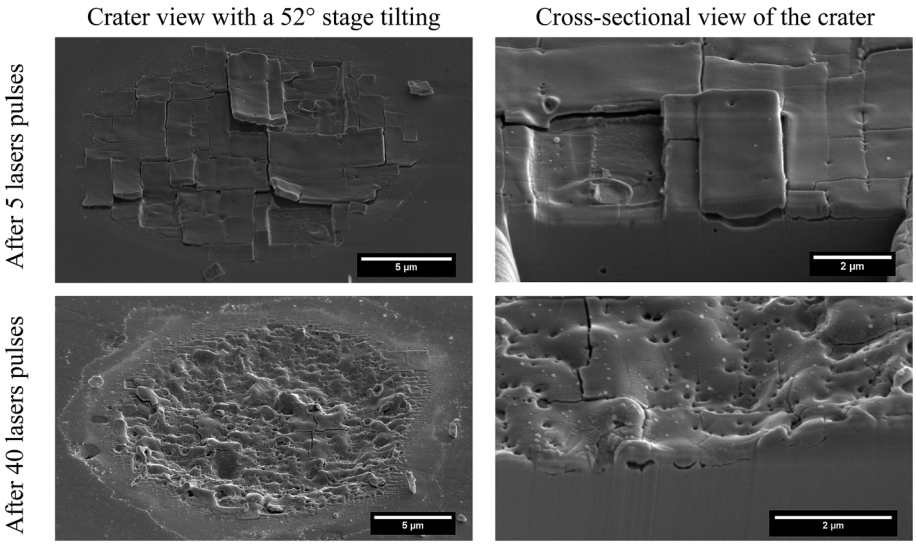

Fig. 2 High-resolution scanning electron microscope (SEM) images of the reference UO_2 single crystal after 5 and 40 laser pulses having a fluence of 0.24 J cm^{-2} each. Cross-sectional images of the ablation craters were generated after milling of lateral trenches using a focused ion beam (FIB) microscope.

reason why the first data points displayed in Fig. 1A had a large deviation from linearity, in particular at high single shot fluence.

Depth assessment of LA craters

A confocal laser scanning profilometer was used to measure the physical dimensions of the laser ablation craters. A representative example of such a circular laser ablation crater with a 25 μm nominal diameter after 40 laser shots on the reference UO_2 single crystal is shown in Fig. 3A. While the scale of both axes in Fig. 3A is given in μm, one has to consider the aspect ratio in this figure. A small change in the depth of the ablation crater is reflected by a comparatively large distance on the *y*-axis and *vice versa* for the distance plotted on the *x*-axis. The conical shape of the crater, typical for ns-laser ablation systems,[3,6] leads to partial mixing of consecutively ablated layers of the crater and thereby limits the obtainable depth resolution. The use of a state-of-the-art fs-laser ablation system improves substantially both the crater shape and depth resolution.[3,8,13]

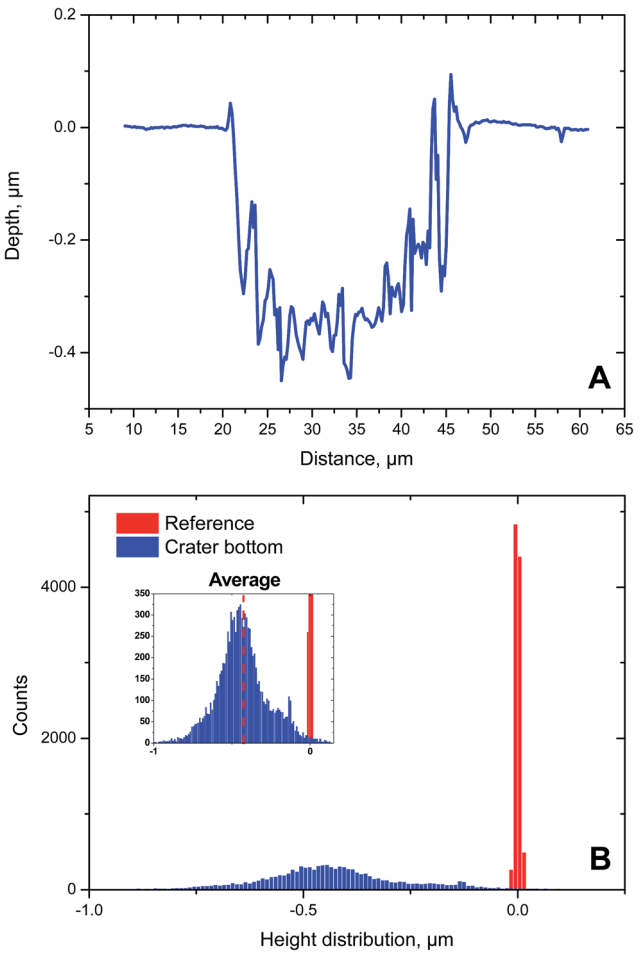

Fig. 3 Characterisation of the laser ablation crater of the reference UO_2 single crystal after 40 laser pulses providing a fluence of 0.24 J cm^{-2} each, using a confocal laser scanning profilometer. (A) Representative depth profile of a LA crater. (B) Height distribution of a reference area (red) and of the crater bottom (blue) used to calculate the average step depth. See text for details.

As the laser is not removing matter from the UO_2 single crystal layer by layer, the crater bottom is not flat, but largely uneven (Fig. 3A). Consequently, this leads to a measurable difference between the maximum depth (0.47 μm) and the average depth (0.43 μm) of the LA crater (Fig. 3A). And the variability in the assessment of the crater depth, in turn, will impact the calculation of the laser ablation rate, for example. To circumvent the above-mentioned issue, the concept of *average step depth* is employed frequently in this context. The average step depth, or more generally, the average step height, is a methodology to calculate the height difference between two surfaces. This approach is particularly effective when, due to the high level of roughness, it is not possible to define a mathematical plane representing the two surfaces.

To this end, two regions within the sample were selected, the first one (hereafter named "reference") representing the zero level, while a second one represented the "crater bottom". An absolute height value was assigned to all pixels of the generated computer image of the surfaces of these two areas, obtaining two height distributions. Since only the height difference of the two levels is of interest, the absolute height scale was shifted by a constant factor bringing the average of the reference height distribution to a value distributed around zero. In Fig. 3B the height distributions of both the reference area (red) and one of the deepest craters (blue) ablated on the reference UO_2 single crystal SC1 are shown. The red histogram is very narrow because the corresponding pristine surface of the single crystal was mirror-polished prior to LA-MC-ICP-MS analysis. By contrast, the blue distribution, representing the crater bottom, was broad in comparison, ranging from almost −1 μm to even slightly positive values. This broadening is indeed the direct consequence of the ablation-induced roughness. Despite this broad height distribution, the calculation of the average of the distribution allowed the assignment of an individual depth value to each LA crater in the most unbiased way. All depths reported here are expressed as average step depth.

Laser ablation crater diameter

The confocal laser profilometer also served for the characterisation of surface features such as the diameter of the generated LA craters of the reference UO_2 single crystal SC1. To this end, a circle defining the LA crater needed to be established. To minimise operator bias when defining a circle corresponding to the crater being measured, the analysis software offers the so-called multi-point approach which enables the operator to select a redundant number (8) of points lying on the laser footprint. The software then automatically defines the circle which passes closest to the selected points.

In this way, the diameters of all LA craters of the reference UO_2 single crystal SC1, generated with an increasing number of laser shots, were measured. This experiment, repeated on five individual spots, revealed expanding crater diameters with increasing number of laser pulses indicated as cumulative fluence in Fig. 4. This suggests a crater edge effect in the case of the presence of a concentration gradient. While this relative trend towards larger crater diameters is obvious, also their absolute

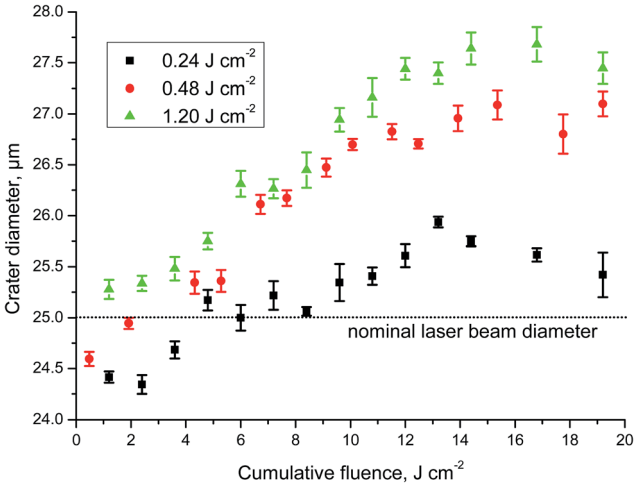

Fig. 4 Assessment of laser ablation crater diameters. Dependence of crater diameter ($n = 5$) of the reference UO_2 single crystal on the applied cumulative fluence using various fluence levels. The nominal diameter of the ablation crater amounted to 25 µm.

values were striking. Note that the nominal diameter of the laser beam was set to 25 µm, while the measured diameters ranged from ~24.3 µm to 27.8 µm (Fig. 4). Additionally, a higher fluence of individual laser shots resulted in larger crater diameters, even though the cumulative fluence was the same for all three experiments, *i.e.,* using pulses of 0.24 J cm^{-2}, 0.48 J cm^{-2}, and 1.20 J cm^{-2}.

Please note that for low laser power, *i.e.,* 0.24 J cm^{-2} and 0.48 J cm^{-2}, crater diameters were lower than the nominal laser beam diameter at low cumulative fluence. As the minimum selectable power (0.1% and 0.2% of the maximum nominal power) was considered here, the interaction of the laser beam with the UO_2 single crystal at the first few laser shots was not sufficiently intense to generate craters that have the dimensions of the laser beam at least. The small standard deviations on the average of five replicate measurements, however, reveal the highly reproducible behaviour of this laser/matter interaction (Fig. 4).

While the pattern of increasing crater diameters was very similar for laser fluence settings of 0.48 J cm^{-2} and 1.20 J cm^{-2}, the lowest laser fluence adjustment of 0.24 J cm^{-2} yielded a somewhat different pattern with lower crater diameters (Fig. 4). Starting from a cumulative fluence of ~11 J cm^{-2}, crater diameters tended to remain constant and did not further increase with increasing cumulative fluence. Taken together, this experiment highlighted the impact of the way the energy of individual laser pulses is delivered towards the sample surface, even though the total amount of energy, *i.e.,* cumulative fluence was identical for all three experimental settings. In other words, delivering the same amount of energy to the sample surface, but in various individual laser energy packages produced different crater diameters.

To ascertain the accuracy of the absolute values of the crater diameters, the x- and y-calibration of the profilometer was regularly checked and confirmed with two calibrated references.

Influence of laser focus on ablation crater geometry

Accurately focusing the laser beam on the sample surface is not always straightforward, especially if the specimen is black and mirror-polished, such as the UO_2 single crystals in this study.

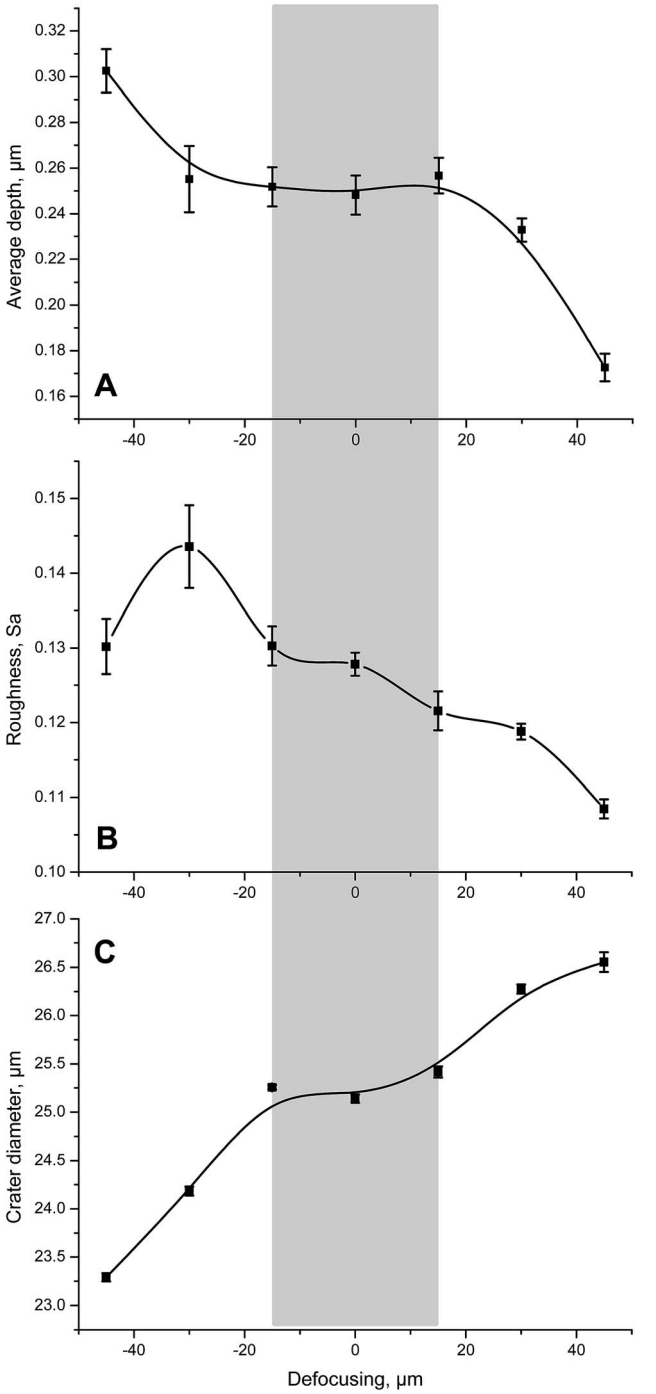

Fig. 5 Influence of laser focus on the average depth, surface roughness and crater diameter as determined on the reference UO_2 single crystal. Each data point represents the average of five replicate measurements after application of 40 laser shots having a fluence of 0.24 J cm^{-2} each. The grey area represents the laser focus region from −15 µm to +15 µm in which all three investigated parameters remain reasonably constant.

Therefore, the potential influence of the beam being out of focus upon the laser-UO_2 surface interaction was investigated in more detail. Initially the laser beam was focussed as accurately as possible onto the surface of the reference UO_2 single crystal SC1, which was then followed by shooting 40 laser pulses of 0.24 J cm^{-2} each. Subsequently, the average depth and diameter of ablation craters were assessed together with the corresponding surface roughness of the bottom of the crater. This experiment was repeated five times and served as a reference point for data obtained when the laser beam was out of focus. Following this, the laser beam was stepwise defocussed by 15 μm, 30 μm, 45 μm, −15 μm, −30 μm, and −45 μm and the above procedure was repeated.

The outcome of this investigation is graphically summarised in Fig. 5. In general, a defocussing of the laser beam by ± 15 μm had almost no impact on any of the three investigated parameters as indicated by the grey area in Fig. 5. Changing the focus of the laser beam from +45 μm to −45 μm, however, increased the laser ablation rate and surface roughness by as much as ~75% (Fig. 5A) and ~20% (Fig. 5B), respectively. Concurrently, the crater diameter decreased by about ~13% (Fig. 5C). Taken together, small inaccuracies (±15 μm) of the laser focus will not systematically bias the laser ablation rate, surface roughness and crater diameter, while larger defocussing certainly will have an impact.

Depth profile of UO_2 single crystals having different ^{235}U gradients

To establish U self-diffusion coefficients in UO_2 single crystals, depth profiling with secondary ion mass spectrometry (SIMS) has been applied in the past.[25] Similarly, laser ablation microprobe (LAMP)-ICP-MS was employed to study the diffusion of U in solid cement monoliths.[26]

For an appropriate investigation of U self-diffusion in UO_2 single crystals, the depth profiling capabilities of the laser ablation system were applied to the two UO_2 single crystals SC2 and SC3, both featuring a uranium isotopic concentration gradient (^{235}U enriched on the surface and depleted in the bulk). Several repetitions of the LA experiment (8 for SC2 and 10 for SC3) were performed applying the same laser parameters (diameter, fluence, repetition rate and wash out delay) as used for the analysis of the reference UO_2 single crystal SC1. The acquired data stream from the LA-MC-ICP-MS measurements was evaluated using home-made single-shot data evaluation software.

The surface layers of both investigated UO_2 single crystals consisted of enriched U (~21 wt% to 26 wt% ^{235}U) that diffused into the depleted body of the specimens (Fig. 6). The relative standard deviation of the average of five consecutive measurements ranged from ~3 to ~6% for the first 13 data points of the depth profiles of both UO_2 single crystals where the largest and most relevant changes in the $n(^{235}U)/n(^{238}U)$ amount ratio were seen (Fig. 6), increasing to about 12% for replicate measurements of depleted U, *i.e.,* the base material. It is important to note that this precision was fit-for-purpose for this study. The limiting factor for the overall analytical performance was the reproducibility of the removal of the sample material with the laser ablation rather than the measurement precision.

The experimental conditions (reaction temperature, O_2 partial pressure, *etc.*) applied during the preparation of the test samples revealed only a small impact on the diffusion of ^{235}U into the two UO_2 single crystals. While a discussion of more technical details is beyond the scope of this study, the developed analytical procedures will be employed to study the diffusion behaviour of U into UO_2 with the goal of setting up diffusion coefficients for this material.[1] Due to the presence of a brittle thin top layer left from sample preparation, it was not possible to derive a unique laser ablation rate for the two UO_2 single crystals SC2 and SC3. The variability of the thickness of this layer was strongly affecting the laser ablation rate. Consequently, a serious quantification of this parameter was not possible for these two specific samples. For this reason the $n(^{235}U)/n(^{238}U)$ amount ratio in Fig. 6 is presented as a function of the laser pulse number. The use of an uncalibrated depth axis (*x*-axis) in Fig. 6, however, may reduce the potential difference in diffusivity between the two samples.

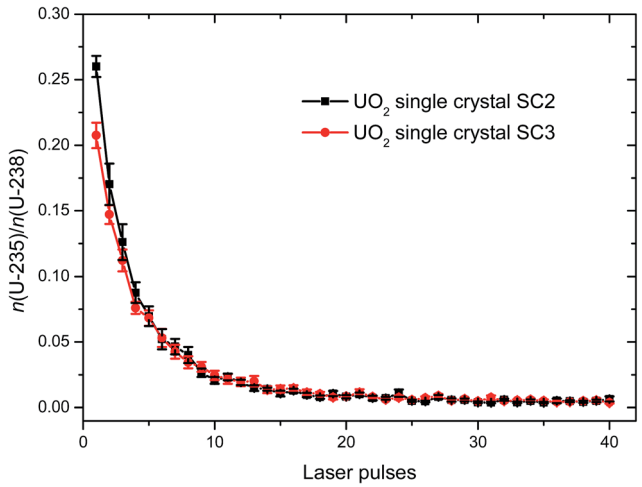

Fig. 6 In-depth $n(^{235}U)/n(^{238}U)$ amount ratios ($n = 5$) measured for the two UO_2 single crystals SC2 and SC3 revealing penetration of ^{235}U into the bulk material.

Conflicts of interest

There are no conflicts to declare.

Acknowledgements

The authors gratefully acknowledge the U isotopic analysis of a fragment of the investigated reference UO_2 single crystal using TIMS by the Analytical Service of JRC Karlsruhe.

References

1 Y. Ma, A study of point defects in UO_{2+x} and their impact upon fuel properties, Materials Science [cond-mat.mtrl-sci], Université d'Aix-Marseille, 2017, English. <tel-01714468v2>.

2 J. Pisonero, J. Koch, M. Wäle, W. Hartung, N. D. Spencer and D. Günther, *Anal. Chem.*, 2007, **79**, 2325–2333.
3 J. Pisonero and D. Günther, *Mass Spectrom. Rev.*, 2008, **27**, 609–623.
4 B. Hattendorf, J. Pisonero, D. Günther and N. Bordel, *Anal. Chem.*, 2012, **84**, 8771–8776.
5 V. Grimaudo, P. Moreno-García, A. Riedo, M. B. Neuland, M. Tulej, P. Broekmann and P. Wurz, *Anal. Chem.*, 2015, **87**, 2037–2041.
6 A. Gutiérrez-González, C. Gonzáles-Gago, J. Pisonero, N. Tibbetts, A. Menéndez, M. Vélez and N. Bordel, *J. Anal. At. Spectrom.*, 2015, **30**, 191–197.
7 A. Limbeck, M. Bonta and W. Nischkauer, *J. Anal. At. Spectrom.*, 2017, **32**, 212–232.
8 D. Käser, L. Hendriks, J. Koch and D. Günther, *Spectrochim. Acta, Part B*, 2018, **149**, 176–183.
9 X. Cheng, W. Li, W. Hang and B. Huang, *Spectrochim. Acta, Part B*, 2015, **111**, 52–56.
10 Z. Varga, M. Krachler, A. Nicholl, M. Ernstberger, T. Wiss, M. Wallenius and K. Mayer, *J. Anal. At. Spectrom.*, 2018, **33**, 1076–1080.
11 M. Krachler, Z. Varga, A. Nicholl, M. Wallenius and K. Mayer, *Microchem. J.*, 2018, **140**, 24–30.
12 M. Krachler, Z. Varga, A. Nicholl and K. Mayer, *Analytica Chimica Acta: X*, 2019, **2**, 100018.
13 J.-I. Kimura, Q. Chang, N. Kanazawa, S. Sasaki and B. S. Vaglarov, *J. Anal. At. Spectrom.*, 2016, **31**, 790–800.
14 T. J. Ver Hoeve, J. S. Scoates, C. J. Wall, D. Weis and M. Amini, *Chem. Geol.*, 2018, **483**, 201–217.
15 P. K. Mukherjee, A. K. Souders and P. J. Sylvester, *J. Anal. At. Spectrom.*, 2019, **34**, 180–192.
16 J. M. Cottle, M. S. A. Horstwood and R. R. Parrish, *J. Anal. At. Spectrom.*, 2009, **24**, 1355–1363.
17 D. Magallon, H. Schins, R. Zeyen and R. Hohmann, The FARO experimental programme: quick look on UO_2 melting and BLOKKER I results, *European Commission*, Joint Research Centre, Ispra, 1989.
18 J. Pisonero, D. Bouzas-Ramos, H. Traub, B. Cappella, C. Alvarez-Llamas, S. Richter, J. C. Mayo, J. M. Costa-Fernandez, N. Bordell and N. Jakubowski, *J. Anal. At. Spectrom.*, 2019, **34**, 655–663.
19 A. J. Managh and P. Reid, *J. Anal. At. Spectrom.*, 2019, **34**, 1369–1373.
20 O. B. Bauer, O. Hachmöller, O. Borovinskaya, M. Sperling, H.-J. Schureck, G. Ciarimboli and U. Karst, *J. Anal. At. Spectrom.*, 2019, **34**, 694–701.
21 T. Pettke, F. Oberli, A. Audétat, U. Wiechert, C. R. Harris and C. A. Heinrich, *J. Anal. At. Spectrom.*, 2011, **26**, 475–492.
22 M. Klaver, R. J. Smeets, J. M. Koornneef, G. R. Davies and P. Z. Vroon, *J. Anal. At. Spectrom.*, 2016, **31**, 171–178.
23 F. Claverie, A. Hubert, S. Berail, A. Donard, F. Pointurier and C. Pécheyran, *Anal. Chem.*, 2016, **88**, 4375–4382.
24 S. R. Lewis, A. Simonetti, L. Corcoran, T. L. Spana, B. W. Chung, N. E. Teslich and P. C. Burns, *J. Radioanal. Nucl. Chem.*, 2018, **318**, 1389–1400.
25 A. C. S. Sabioni, W. B. Ferraz and F. Millot, *J. Nucl. Mater.*, 1998, **257**, 180–184.
26 D. Sugiyama, T. Chida and M. Cowper, *Radiochim. Acta*, 2008, **96**, 747–752.